Journal Pre-proof

Influence of Process Parameters in AFP Fiber Steering on Cylinders: Constant Curvature Paths

Roudy Wehbe, Christopher Sacco, Anis Baz Radwan,
Mazen Albazzan, Ramy Harik

PII: S2666-6820(20)30036-0
DOI: https://doi.org/10.1016/j.jcomc.2020.100036
Reference: JCOMC 100036

To appear in: *Composites Part C: Open Access*

Received date: 15 June 2020
Revised date: 21 July 2020
Accepted date: 2 September 2020

Please cite this article as: Roudy Wehbe, Christopher Sacco, Anis Baz Radwan, Mazen Albazzan, Ramy Harik, Influence of Process Parameters in AFP Fiber Steering on Cylinders: Constant Curvature Paths, *Composites Part C: Open Access* (2020), doi: https://doi.org/10.1016/j.jcomc.2020.100036

Influence of Process Parameters in AFP Fiber Steering on Cylinders: Constant Curvature Paths

Roudy Wehbe, Christopher Sacco, Anis Baz Radwan, Mazen Albazzan, Ramy Harik

McNAIR Center for Aerospace Innovation and Research, Department of Mechanical Engineering, College of Engineering and Computing, University of South Carolina, 1000 Catawba St., Columbia, SC, 29201, USA

Abstract

Automated Fiber Placement (AFP) is a flexible manufacturing technique which allows the manufacturing of complex layups where steered paths are necessary to achieve the surface coverage. However, steering tows using the AFP process introduces challenges in terms of quality and productivity due to steering induced defects. The quality of AFP layup is highly dependent on the geometry and the curvature of the path as well as the manufacturing process parameters such as layup temperature, head speed and compaction force. Understanding how these parameters affect the process is important to achieve the desirable quality of the final part. In this paper, several paths are steered at different radii of curvature (1270, 635 and 318 mm) on a cylindrical tool using different combinations of process parameters. The quality of the obtained layup is assessed through image processing of acquired profilometry scans. In-plane tow displacement and out-of-plane tow deformations are captured over the length of each placed course. Using numerical techniques, the defect occurrence is correlated to the input process parameters. Results show that the path curvature is the main feature driving defect formation. The remaining process parameters are ranked according to their influence.

Keywords: Automated Fiber Placement, Fiber Steering, Process Parameters, Inspection, AFP Defects

1. Introduction

Carbon fiber composites are increasingly becoming the reigning material of choice in many industries, especially aerospace, with automated fiber placement (AFP) being a cornerstone in the manufacturing process of airplane structures. AFP is a manufacturing technique that utilizes carbon fiber tows, which can have a matrix phase of thermoset or thermoplastic, to additively create a composite structure layer by layer. Sometimes these complex structures contain curvatures resulting in the need to steer the tows to follow the surface contours and achieve full coverage [1]. In other cases, tow steering can be intentional in the design to enable the fabrication of optimized variable stiffness layups [2, 3], especially for the case of cylinders.

Tatting was the first to investigate the design of variable stiffness cylindrical shells to identify possible areas of improvement that may be accomplished with fiber-steered laminates [4]. Blom et al. also demonstrated that fiber steering with circumferential tailoring can increase the buckling load of cylindrical shells under bending while subjected to the Tsai-Wu strength constraint [2]. The maximum curvature constraint was accounted for in the design process to reduce the defects that can be obtained during AFP manufacturing. In Rouhi et al. [5] showed an improvement of 18.5% in the buckling load of a variable stiffness cylinder under bending compared to a constant stiffness couterpart. Khani et al. also utilized fiber-steered laminates to maximize the buckling load of general cross section cylinders under axial compression and bending with strength constraints [3]. In addition, Sun et al. show that fiber steering can improve the buckling loads of elliptical cylinders in pure compression using a circumferential stiffness variation [6]. Albazzan et al. also demonstrate that fiber steering is essential in the design of cylinders with holes under bending to increase the buckling capacity. This can be achieved by reducing the stress concentrations and redistributing the loads of the structure [7, 8].

However, the improvements come at the expense of an increased design complexity subject to AFP manufacturing constraints. A major manufacturing

Defect	Description	Cause
Gap	Unoccupied space between tows	Steering errors or layup on a complex tool
Overlap	Placement of a tow onto an adjacent tow	Steering errors or layup on a complex tool
Wrinkle	Wavy pattern at the boundaries of a tow resulting in only partial tool contact	Small steering radius; Overfeeding material
Twist	A tow rolled axially 180 on itself and then compacted by the roller	Friction between guide holes or overly tacky tows; Fold propagation
Missing Tow	An entire tow falls off the tool or is never applied	Material feed error; Adhesion problems
Splice	Two tows are joined end-to-end so that they overlap	Result of finite length slit tape for forming tows
Pucker	Lifting up of a tow from the tool surface along the tow width	Overfeeding material; Machine error

Table 1: A Number of AFP Defect Types Identified in Harik et al. [9]

constraint for fiber-steered variable stiffness laminates is the minimum steering radius, below which defect can occur during the process. In addition to fiber-steering related defect, a range of other defect can occur during production such as gaps, overlap, twists, wrinkles and others [9] (Table 1) since the AFP manufacturing process has not been perfected yet. It is the author's intention to facilitate discussions on the evaluation and analysis of manufacturing of steered tows on a cylinder.

1.1. Steering in AFP

In addition to typical defects that occur during a regular AFP manufacturing program, specific defects induced by tow steering also can occur depending on the steering radius and the processing parameters (mainly layup speed, temperature, and applied compaction). The origin of these defects is the mismatch in length between the fibers within the tow and the curved path on the surface. This mismatch in length has to be absorbed through a deformation mechanism. These tow deformations are split into three categories[10, 11, 12]: strains (tensile, compressive and shear), large in-plane deformations (waviness and bunching), and large out-of-plane deformations (wrinkling and folding). Usually, large deformations are considered as critical defects, and thus restricting the manufacturing process. A geometrical model for tow wrinkles in AFP is presented in [13], where for a given layup, the amplitude of the wrinkles can be approximated and critical locations can be determined.

However, depending on the applied process parameters and the achieved level of adherence (tackiness) between the tow and the substrate, large out-of-plane tow deformations can be suppressed to other favorable deformations. This is usually accomplished experimentally, by varying the process parameters and observing the obtained defects, such as the work reported in [14, 15, 16, 17]. In these experiments, defect assessment is done visually, and an exact measurement of the amount of defect is usually not reported. In [12], the stereo digital image correlation technique (StereoDIC) is used to measure shape and strain deformations for tows steered at different radii of curvatures. However, defects such as folds can obscure the speckled pattern at the top surface of the tow and measurements cannot be obtained. In [18], profilometry scans of steered paths on a flat surface are used to observe the out-of-plane defects as well as gaps between the tows. Based on these observations, a qualitative assessment regarding the optimum process window is recommended for the specific used material.

1.2. Composite Inspection

Due to their low contrast, the imaging of composite materials for defects has proved difficult in the past. Surface and subsurface defects manifest in a number of ways, and thus finding methods for imaging analysis must be equally as broad. Generally, conventional visual spectrum images are not viable as an inspection technology. The low contrast, particularly of carbon composites, makes feature identification challenging. However, laser profiling, thermal imaging, eddy current inspection, and a number of other additional non-conventional imaging techniques have had great success in the non-destructive testing (NDT) process.

Thermographic-based composite inspection begins with the excitation of material through a heat source. This is typically accomplished through the use of a halogen lamp, however LED heat sources have also been used [19]. The propagation of heat through a structure is almost entirely dependent on material properties, and thus where those properties have changed due to damage heat transfer will occur differently from the background material. As this transfer is taking place, thermal cameras capture the differences and produce an image of the structure under inspection. Two variations of the thermographic techniques are lock-in and long pulse thermography. Lock-in implies that detection and excitation are happening simultaneously in a pulsed pattern, which results in higher quality thermographic images [20].Long pulse thermography involves the extended excitation of the structure, which can be useful in poorly conducting materials such as composites [21].

Profilometry is another popular NDT technique most often utilized in the 3-dimensional rendering of a surface. A laser pattern is projected down onto a surface, through which surface features are inferred from deviations in the pattern [22]. The advantage of profilometry is the rapid profiling of a surface without the need to take surface contrast into account.

In the context of AFP, recent inspection techniques [23, 24, 25] are pushing towards complete characterization of defects, where depending on their severity, decisions for the time-consuming repairs can be made. In addition, there is a significant push for thermographic in-situ inspection in AFP for thermosetting

materials [26, 27]. Several researchers have noted the large down-time in AFP production due to manual inspection and rework [28, 29, 30]. However, the advantages with automated AFP inspection are not simply limited to cycle-time improvements. The digitization of the inspection process also leads to the capture of data that can then be used to further inform the manufacturing process. Automated defect capture enables the long term tracking of key metrics, thus making it a large step towards the digital twinning of the entire AFP process.

1.3. Research Focus

This document aims to explore the relationship between manufacturing and design parameters on cylindrical steered courses and their relationship to the production of defects. By using a profilometery-based inspection system with a novel defect characterization approach, an exact quantitative measurement of defect production can be obtained. From this measurement, statistical representations of the connection between various process parameter configurations and defect production can be observed. In this paper, the manufacturing of steered courses on a cylindrical mandrel is considered, adding several challenges compared to steering on flat surfaces. From a kinematic standpoint, the 3D steered paths on the cylinder are more challenging to manufacture and require the engagement of the 7th axis of the AFP machine (rotating mendrel) as opposed to steering on a stationary flat surface. In addition, due to the surface curvature of the cylinder, the pressure and temperature distribution across the width of the roller may be nonuniform compared to fiber placement on flat surfaces. The experimental procedures including course geometry and process parameters are discussed in section 2. The in situ measurements of the layup temperature, speed, and profilometry images showing the obtained defects are reported in section 3. Using image processing techniques, those defects are extracted, quantified for each placed course, correlated to the measured process parameters and presented in section 4. Finally, conclusions, recommendations, and possible future work are presented in section 5.

2. Experimentation

2.1. Steering Design

For the steering experiment on the cylinder, three types of curves are considered: constant curvature arcs at 1270, 635, and 318 mm respectively. In order to design these paths on the cylindrical surface, the differential geometry steps described in [31] are followed. First, an arc-length parametric definition of the cylinder's surface is determined as a function of the circumference c, the cylinder's length z, and the radius r ($r = 610\ mm$):

$$\begin{aligned} cylinder(c,z) &= \left\{ rcos\frac{c}{r}, rsin\frac{c}{r}, z \right\}, \\ 0 \leq c &\leq 2\pi r, \\ z_{min} \leq z &\leq z_{max}. \end{aligned} \tag{1}$$

To obtain the curved paths on the cylinder's surface, a 2D particularization $\{x(s), y(s)\}$ of the constant curvature arcs is used as follows:

$$\{x(s), y(s)\} = \{\rho sin(as+b)+d, \rho cos(as+b)+e\}, \tag{2}$$

where ρ corresponds to the steering radius of the path (1270, 635, and 635 mm) and the constants a, b, d, e are chosen so that $\{x(s), y(s)\} \in \Omega$ the rectangular domain of definition of the flattened cylinder bounded by the minimum and maximum of the circumference c and the cylinder's length z (see Figure 1). Then, the mapped curved path on the cylinder's surface can be obtained by substituting the circumference c and length z with $x(s)$ and $y(s)$ respectively:

$$Curve3D(s) = cylinder\left(x(s), y(s)\right). \tag{3}$$

The obtained paths bounded by the domain of definition of the flattened cylinder and their corresponding mapped 3D paths on the cylinder's surface are visualized in Figure 1 and Figure 2 respectively. Using the above transformation from the 2D domain to the 3D cylinder's surface, the geodesic curvature of the paths on the cylinder coincides with the 2D curvature of the paths, hence the mismatch in length between the edges of the tow-path remains the same.

However, the total curvature of the paths is different due to the contribution of the normal curvature of the cylinder. This results in a more challenging manufacturing process from a kinematics standpoint, and leads to a nonuniform distribution of pressure and temperature across the roller width.

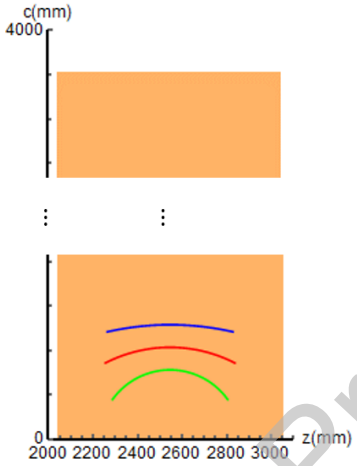

Figure 1: Steered paths on flattened cylinder

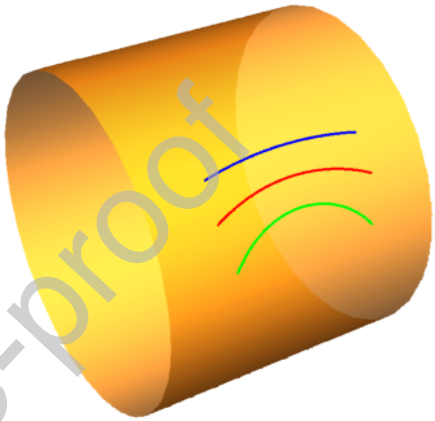

Figure 2: Steered paths on cylinder

2.2. Programming

The generated 3D curved paths in the design section are sampled at 3 mm spacing along the length s and exported to CATIA as a cloud of points. The curves are then reconstructed and projected on the tool surface. Additional linear portions are added tangentially to the paths on each side and extended to cover the boundaries of the cylinder. A total of 9 courses are programmed for each curved path. The courses are spaced by applying rotations and mirroring options in the CAD software so that the cylinder's surface is covered without overlapping between the courses. The designed courses are visualized in figure 3.

Instead of laying the steered paths directly on the cylinder's metallic surface, two 90°hoop plies are placed first as a substrate. If these plies were to be placed

at exactly 90°, the courses need to be cut along a certain line along the cylinder's length. Instead, a small angle deviation is allowed so that a single course can wrap the entire cylinder's surface. Using geometrical relationships, the deviated angle is found to be a function of the course width, the inter-band offset (offset distance between adjacent courses) and the mandrel's circumference. Based on these parameters, the calculated ply angle of the substrate is 89.224°. The two substrate plies are added in opposite directions (±89.224°) with an adequate stagger shift to remove any gaps that might occur. The steering experiments are performed as a third ply.

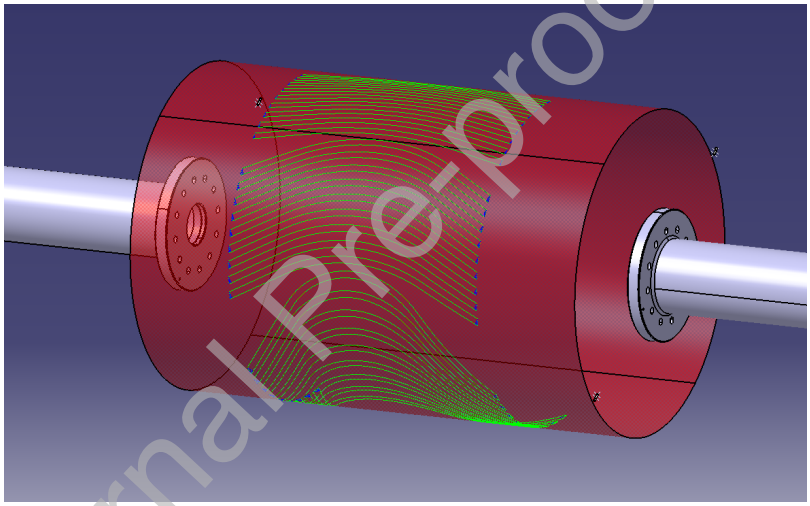

Figure 3: Programmed constant curvature arcs on cylindrical mandrel

2.3. Manufacturing Equipment

2.3.1. AFP Machine

The courses were deposited using an Ingersoll Machine Tools (IMT) Lynx AFP machine [Figure 4a] located at the McNair Center. Machine motion is controlled through a Siemens 840D Powerline controller and a Siemens Simatic300 PLC. The Lynx is a gantry style AFP machine, with a 3+3 axis configuration. The first three axes of motion are derived from linear rail motion with the other 3 axes coming from rotational movement of the machine head. An additional

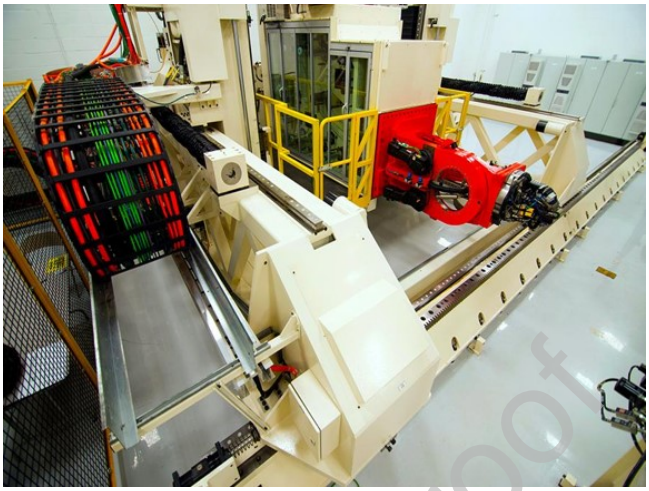

(a) Ingersoll Machine Tools Lynx AFP Machine

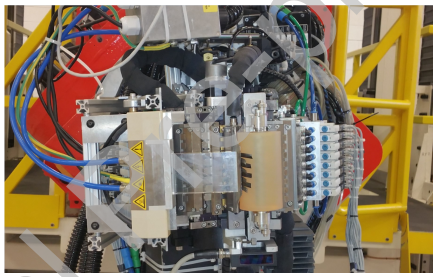

(b) Heraeus Humm3 Heater During Layup

Figure 4: McNair Center AFP Layup Equipment

axis comes from a rotating mandrel. The material used during the experiment is 6.35 mm (1/4 in) Cycom 5320-1, T650-35, 6K, 145 gsm, 33% RW unidirectional tape from SOLVAY. During each course, 4 tows are placed simultaneously along the designed paths using a 50.8 mm wide roller with a hardness of 50. For heating the material, a focused pulsed-light heater supplied by Heraeus denoted as the Humm3 was used [Figure 4b]. The Humm3 is a xenon light heater capable of reaching a power of 6 kW. A crystal is used to distribute the heat across the the layup surface.

2.3.2. Inspection

In the AFP manufacturing cell, an inspection robot referred to as the Advanced Composite Structures Inspection System (ACSIS) is provided for data capture [Figure 5a]. ACSIS is also an IMT product intended to decrease inspection and rework time in the AFP process. The entire system consists of a Kuka KR120 robotic arm actuating 4 Keyence LJ-7080 blue-light laser profilometers and a central computer for data processing. The profilometers are capable of scanning a surface and rapidly generating a height profile across the surface. Once a height profile has been generated, it is then compressed into a greyscale image with pixel values ranging from 0 to 255 [Figure 5b] to be analyzed with the internal ACSIS defect identification algorithms based on machine learning. ACSIS is a ply-by-ply scanning solution in which layup of a single ply is accomplished using the AFP machine and the mandrel is then rotated to be accessible to the ACSIS system operating on an external rail. Once scanning is done, the mandrel rotates back into position and another ply is placed.

2.4. Process Parameters

The main process parameters investigated in this paper are the layup speed (S) (or also referred to here as feedrate), the compaction pressure (P), and the layup temperature (T). For a layup that involves all 7-axis of the AFP machine, the feedrate can be described as the speed at which the material is exiting the machine head and deposited on the surface. This speed is a combination of both the AFP head motion and the rotational speed of the mandrel. In a first step, a baseline for each parameter that yields a successful layup with minimum desirable quality is needed. To achieve that, a random grid search is used and the effect of the parameters is observed. Accordingly, the parameters are varied one at a time to note how the layup is affected and to distinguish between the effects of each parameter. For the layup speed, six different levels are investigated: 6, 10, 20, 30, 50, and 100% of the programmed speed of $25,000\ mm/min$. Concerning the layup temperature, the Humm3 heater attached to the AFP head is used where voltage, frequency and pulse duration of the light source

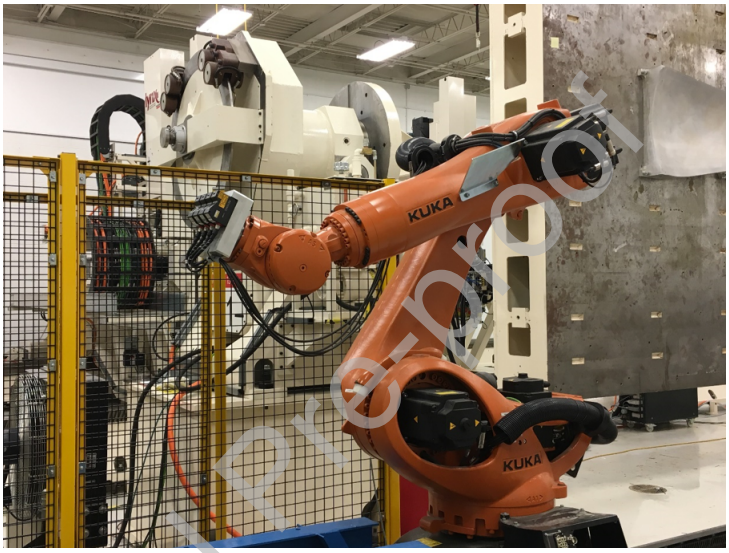

(a) ACSIS Kuka KR120 and Laser Profilometer Configuration

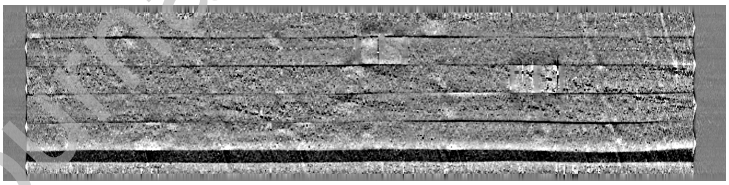

(b) An ACSIS Scan Image

Figure 5: ACSIS Automated Inspection System

can be changed to control the power output and hence the layup temperature. For the purpose of this experiment, the frequency and pulse duration are kept constant at 60 Hz and 2000 μs respectively, and only the voltage is changed at the following levels: 150, 170, 180, and 190 Volts (V). These settings result in a power output of 2, 3, 3.6, and 4.4 kW respectively. The compaction force of the roller is also varied at the following levels: 178, 300, 445, 600, and 750 N. These parameters are summarized in Table 2.

Parameters	Levels					
Compaction force (N)	178	300	445	600	750	
Heater Voltage (V)	150	170	180	190		
Feed rate (%)	6	10	20	30	50	100

Table 2: The parameters and levels considered in the steering experiments on the cylinder

These parameter ranges also make intuitive sense. The lowest level of the compaction force corresponds to the minimum that can be set by the machine, whereas it is not recommended to go beyond 750 N for the type of the roller used. As for the heater, using a voltage below 150 V does not provide enough power for the material to adhere to the surface, whereas voltages beyond 190V resulted in excessive heating of the material (and possible degradation) especially at low speeds. The steering experiments are carried individually for each course and having different combination of parameters. The course number, its description, and the process parameter combination (% of speed, compaction force, heater voltage) used during manufacturing are summarized in Table 3.

For process monitoring during the layup, a recording of the layup speed for each course is captured to note any discrepancy between the actual speed of the layup and the programmed/set one. As for the temperature, four thermocouples are placed along the length of the paths to record the change in temperature over time. The thermocouples are placed on the substrate in the middle of the course width and equally spaced along the path. For each set of process parameters, the thermocouples are first attached to the substrate, then the

Course#	Radius (mm)	S (%)	P(N)	T(V)
130	1270	30	600	150
131	1270	50	445	170
132	1270	100	445	150
133	1270	50	445	170
134	1270	100	300	170
135	1270	100	600	170
136	1270	20	600	170
137	1270	20	750	170
138	1270	20	445	170
139	635	30	600	170
140	635	20	600	170
141	635	10	600	170
142	635	10	600	150
143	635	10	750	170
144	635	20	750	170
145	635	50	750	190
146	635	30	750	180
147	635	100	750	190
149	318	10	445	170
150	318	10	300	170
151	318	10	178	170
152	318	50	445	180
153	318	50	445	150
154	318	100	445	180
155	318	6	445	150

Table 3: Course description and corresponding process parameters

course is placed while measurements are recorded, then the course is peeled off, the thermocouples are removed, and a second course is placed at the same

location with the same process parameters for inspection. The presence of the thermocouples on the substrate acts as a site for out-of-plane defects to initiate, and hence they should be removed before scanning. No instrumentation is used to monitor the roller compaction, it was solely set in the machine parameters.

3. Data Acquisition

In this section, the captured data regarding the feedrate and substrate temperature are first discussed. Then, the quality of the manufactured courses is presented through scanned images of the layup and then analyzed to quantify the steering induced defects.

3.1. Feedrate

Usually during AFP experimentation, it is desired to have constant feedrate at the programmed level throughout the deposition of the course. However, in the case of steering (on flat or cylindrical mandrel) it gets increasingly difficult to maintain a constant feedrate especially at the high-speed settings. This occurs due to the increased complexity in the motion of the AFP head, where more axes are needed to achieve the required paths, which means the motion is more constrained and hence, the feedrate is bound by the speed and acceleration thresholds of the slowest axis (i.e. the axis having the smallest motor). In the case of 0°motion, only the X-axis is involved and therefore the feedrate can comfortably reach up to 25000 mm/min. In the case of steering on the cylindrical mandrel, almost all the axes are involved in the motion. Consequently, during these experiments, the feedrate is not at a constant level, and a continuous monitoring is required. The actual feedrate from the AFP console is recorded, and data points are extracted at $0.1s$ resolution. The results are then plotted with respect to arc-length rather than time. An example of the recorded feedrate for three different configurations of the 1270 mm radius courses (at 100%, 50%, and 20%) is shown in Figure 6. It can be observed that for the course placed at 100%, the target/programmed feedrate is not achieved at any location

within the course due to kinematics restrictions. Instead, significant fluctuations in the feedrate are observed, which would hence cause fluctuations in the nip point temperature. The same behavior is observed for the course placed at 50% except for a brief constant layup feedrate (12500 mm/min) halfway through the course. At 20% of the programmed speed (5000 mm/min), the target feedrate is achieved for the layup resulting in more consistent temperatures.

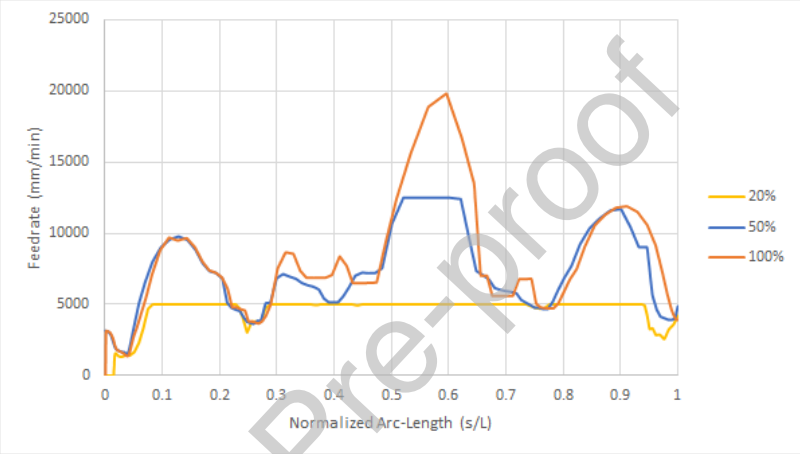

Figure 6: Recorded feedrate at 100%, 50% and 20%

3.2. Temperature

For each of the placed courses, temperature measurements are taken along the length of the path using four thermocouples. A typical measurement of the temperature as function of time is shown in Figure 7 for course 137 (20% speed, 750N compaction, 170V heater voltage). During the layup, the temperature of the substrate experiences a sudden increase just before the tow is fed and compacted on the substrate. When the tow makes contact with the substrate, the temperature drops significantly since the incoming tow from the creel is at a lower temperature than the heated substrate. Then the temperature decays slowly to fall back to the room temperature once the heat is dissipated through the part and the tool. This behavior is observed in all the measurements acquired by the thermocouples.

Naturally, there exists a strong dependency between temperature and feedrate, where at the same power settings the temperature can vary greatly depending on the feedrate used. For the results shown in Figure 7 where course 137 is laid at low speed settings (20% speed), the peak temperatures captured by the thermocouples fall within the same range. Usually, this is not the case where the layup speed fluctuates. Hence, capturing the temperature at only four locations along the length of the path is not enough. Instead, these measurements are used as an indicator of the average temperature.

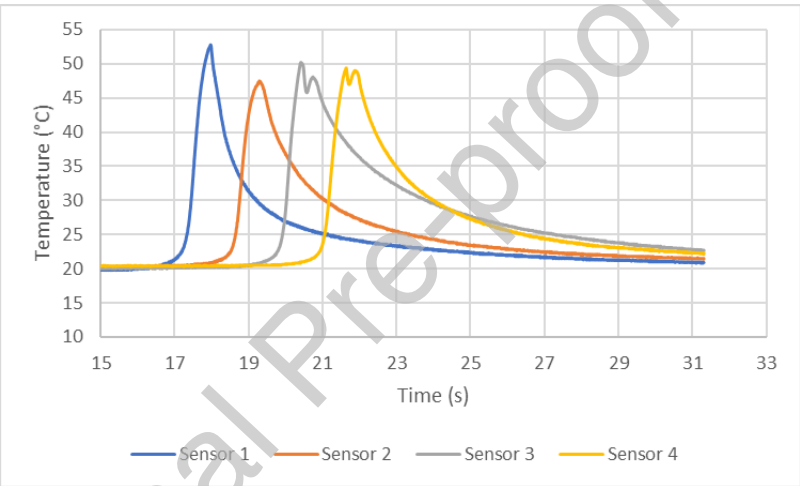

Figure 7: Temperature readings from the thermocouples for course 137

To solve this problem, a series of measurements are performed on courses along the 0°direction, where the speed is varied between 1500 mm/min and 25000 mm/min, at three power levels (150V, 170V, 190V) and three compaction levels (300N, 445N, 600N). Increasing the compaction force leads to an increase in the roller deformation, hence bringing the heater closer to the layup surface which may cause variations in the nip point temperature even for the same power output. Based on the aqcuired measurements, it is observed that different levels of compaction have a minimal effect on the variation in the measured temperature (2-3°C) hence the average of the three measurements is taken and shown in Figure 8 with error bars. This results in a series of temperature

readings from which a relationship between the heater voltage, layup speed, and the maximum nip point temperature can be extracted. This relationship can then be used to predict the nip point temperature for variable courses with variable feedrate. The results for the average measured temperature as function of the layup speed and heater voltage is shown in Figure 8. It can be clearly observed that the relationship between temperature and feedrate is nonlinear and there is a drastic decrease in the substrate temperature as the layup speed is increased.

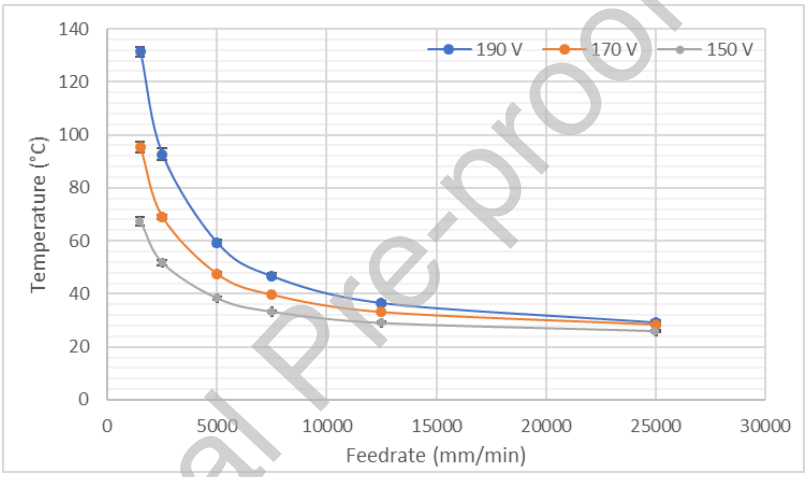

Figure 8: Measured temperature as function of the feedrate

3.3. Quality Assessment

To assess the effects of the parameters and the quality of the process profilometry scans of the layup are captured using the ACSIS system developed by IMT (Figure 9). Several of the authors' previous works have dealt with inspection using the ACSIS system and the identification of novel ways to extract size and shape characteristics from AFP defect scans [23, 24, 25]. Regular photographs of defects as well as photographs through magnifying glass are also captured. An example of these defects is shown in Figure 10 and Figure 11. Different tow deformation mechanisms are observed during this experiment.

Mainly, they can be divided into two categories: large out-plane deformations (wrinkles, tow folds and sheared tows), and in-plane displacement (fiber waviness and tow bunching resulting in gaps between the tows).

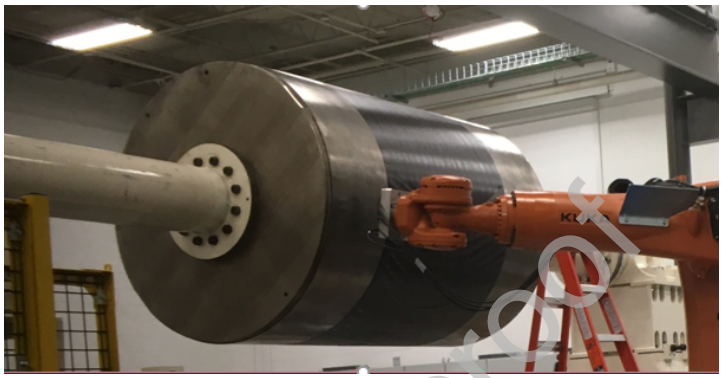

Figure 9: Profilometry scanning of steered layup using ACSIS system

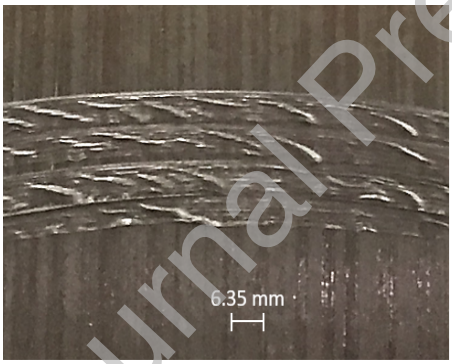

Figure 10: Sheared tows and out-of-plane wrinkles

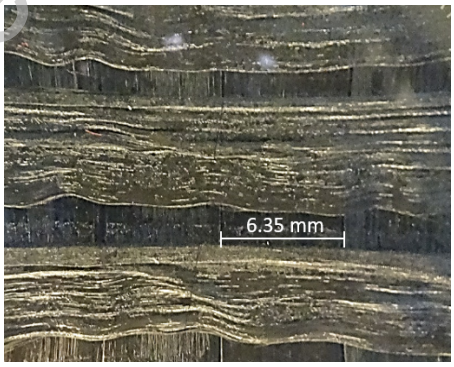

Figure 11: Fiber waviness, bunching and gaps

The linear profilometry scans are visualized in black and white images. An image is generated for each of the 4 profilometers mounted on the robotic arms 5b. These images are later stitched together to reconstruct the surface of the layup. The stitched scans for the placed courses are shown in Figure 12, Figure 13, and 16. It should be noted that the linear scans compress the images in the length direction by a factor of 3.5. This explains why the linear section of the

courses steered at higher curvature are seen with much smaller width compared to the center portion of the course.

By observing the scanned images of the layup, it can be observed visually that the courses steered at 1270 mm radius have the smallest quantity of defects, whereas courses steered at higher curvature experienced severe defects. The types of defects observed during this experiment range from in-plane waviness, bunching, and gaps between tows, to out-of-plane deformations such as wrinkles, folds and sheared tows.

3.4. Defect Detection

The ready abundance of height data draws us towards a relatively simple method for defect identification. By applying simple thresholds to the height profiles and shading in pixels, out of plane deformations and tow displacement can be determined. The lower threshold identifying pixels with values between 0 and 10 represents the tow displacement and the upper threshold, with values between 245 and 255, the out-of-plane tow deformation. The resulting pixel blobs can be extracted using the marching squares algorithm [32], resulting in a bounding polygon around each collection of pixels. From this, small polygons generated from artifacts in the image were filtered out, resulting in a precise bounding polygon being placed around defects of interest. In the case that a significant deformation may cast a shadow that could trigger a false positive, a user interface (UI) developed for previous inspection studies was modified for use with this defect detection paradigm and used to correct errors in the defect detection approach. The UI can export defect information into a JSON file for further analysis. The resulting defects map for the courses steered using different process parameters is shown in Figure 14, Figure 15, and Figure 17 where tow displacements are represented in green and out-of-plane deformations in orange.

3.4.1. Reconstructing Course Geometry

To properly represent this data in the context of the overall course, a center-line must be determined such that the defect can be placed in relation to both

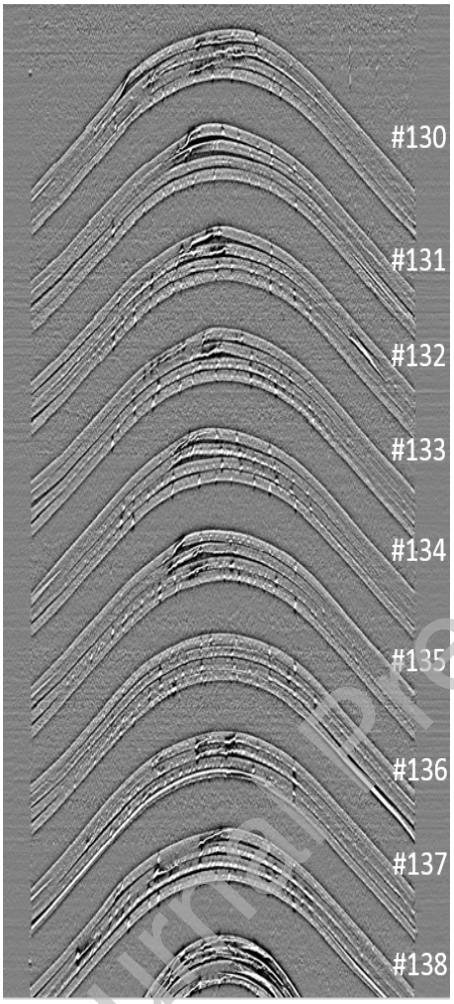

Figure 12: Stitched scans for R1270

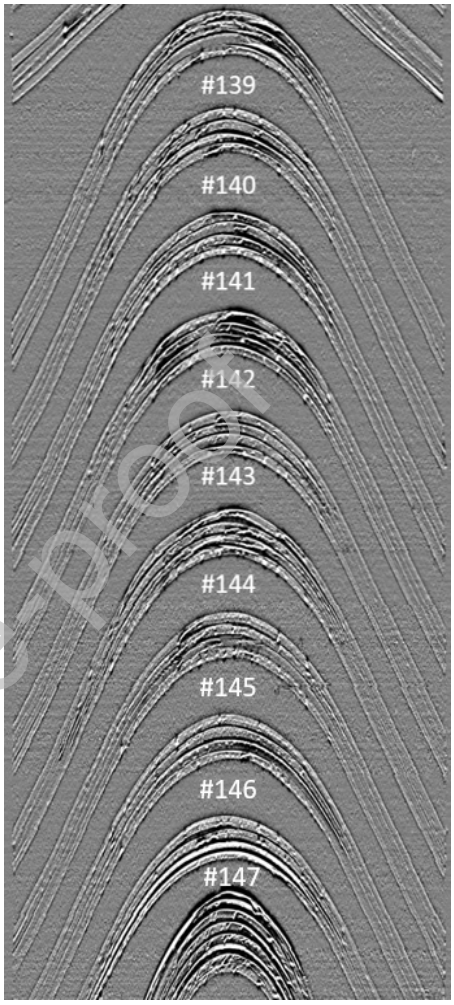

Figure 13: Stitched scans for R635

the course itself, and located according to the width of the course. To generate this centerline, the Voronoi Diagram [33] is created using the course boundaries as seed points [Figure 18]. The Voronoi produces a set of edges that can begin to be thought of as a pseudo-centerline. However, these edges must be filtered and selected from within the larger collection of Voronoi edges. Therefore, edges are filtered to only include those edges that fall within the course. Figure 19a gives an example of these unsorted edges. The pseudo-centerline resulting from

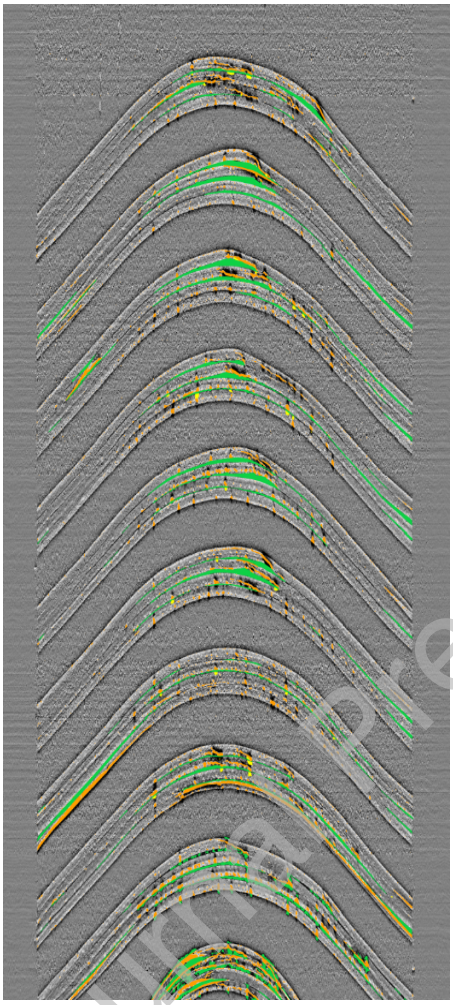

Figure 14: Defect detection for the processed scan of the R1270 courses

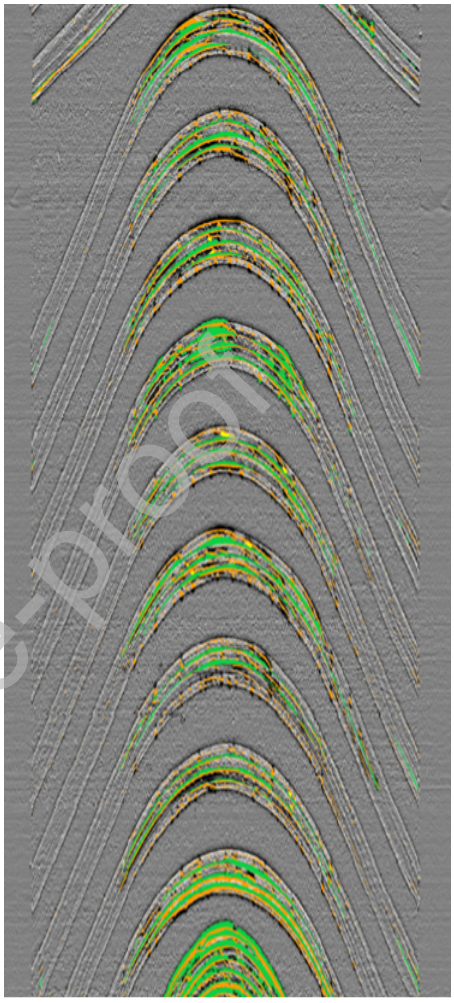

Figure 15: Defect detection for the processed scan of the R635 courses

this filtering process may contain many artifacts that require more processing to remove

These edge artifacts can be removed through a number of potential methods. The authors considered a number of transformational or clustering approaches using the vertices of the edges that could be suitable for the application. However, if one notes a graph reflecting the connectivity of each of the edges, then a

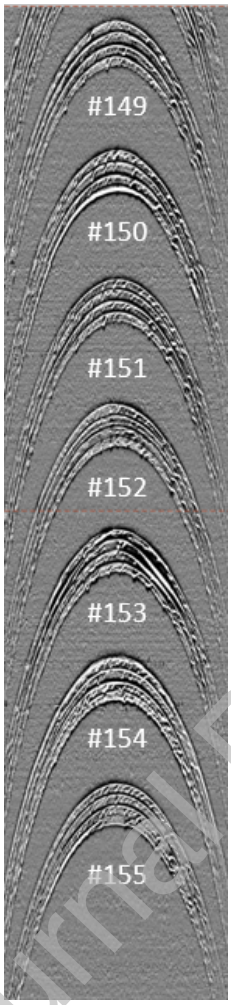

Figure 16: Stitched scans for R318

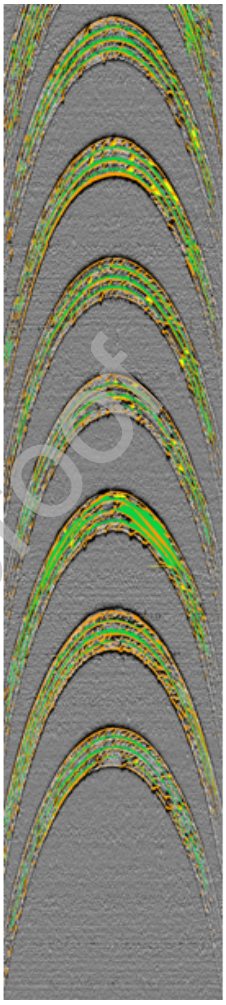

Figure 17: Defect detection for the processed scan of the R318 courses

number of fast graph theoretic approaches can be deployed. To accomplish this, code was created to transform the list of edges from coordinate space to graph space such that connectivity information relating each edge to the overall set of edges could be determined. This produced a graph representing how each edge was bounded to neighboring edges.

Assuming these edge artifacts do not bridge across the interior of our pseudo-

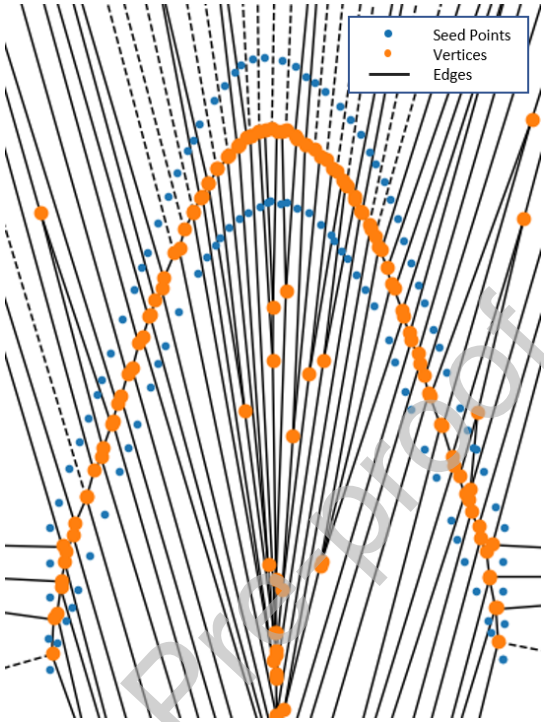

Figure 18: Voronoi Diagram with Course Polygon Vertices as Inputs

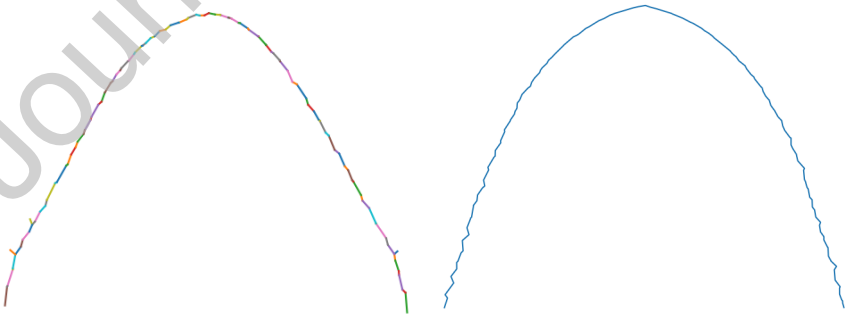

(a) Unconnected Edges within the Course (b) Reconstructed Centerline

Figure 19: Identification of Course Centerline

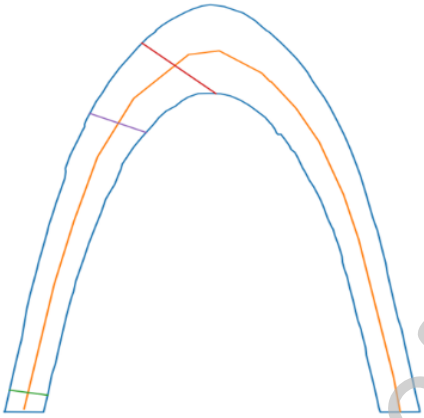

Figure 20: Normal Test Line Across Fitted Centerline

centerline, i.e. the artifacts represent a subgraph that is a simple path, then the centerline approximation is the shortest path from the leftmost to the rightmost edge vertex. This is quickly accomplished using Dijkstra's Algorithm [34] by assuming that all of the edges in the graph have equal weight. Therefore, if the set of edges is small enough such that the process of mapping back and forth between graph space and coordinate space is efficient, then a complete centerline [Figure 19b] can be extracted.

To further improve this centerline description, then a smoothing procedure by fitting a piecewise linear function to the centerline vertices achieves further improvement and importantly improves the smoothness of the centerline when taking the normal to the centerline for defect measurement [Figure 20].

3.4.2. Measurement of Instantaneous Course Quality

To utilize the centerline information and the requisite geometry markers for each course, a line normal to the centerline is created and itterated 1000 times over the length of the centerline. At each point, the length of each defect that intersects with the normal line is measured. The measurement is normalized against the width of the course at the given point, yeilding the fraction of the course at that instant occupied by defects. Moving the normal line across each

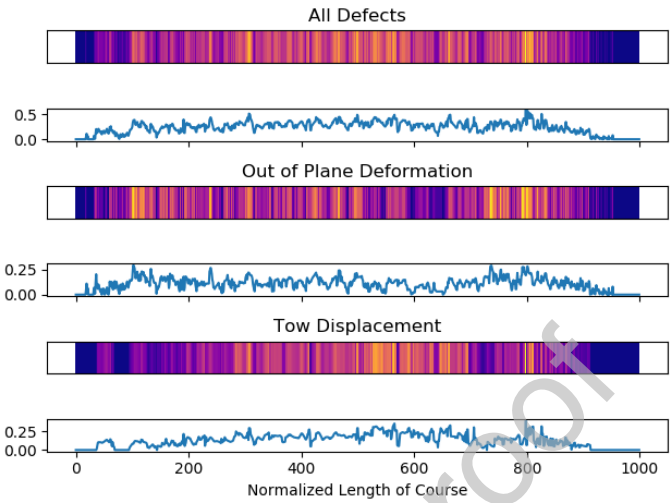

Figure 21: Measurement of Defects Along Course 150

section of the course gives a defect production profile [Figure 21] measuring defects as a function of course length. While the application of this method is restriced to the two defect types of defects concerned in this document, there is little preventing an extension to many types of defects in AFP manufacturing.

3.4.3. Some Initial Data

To assess the influence of the process parameters on the steering induced defects, only the curved portions of the steered paths are considered for analysis. By summing the defects fraction over the curved portion of the path, a percentage of the total area of the course including defects can be obtained. A summary of the calculated percentages for the steered courses are shown in Table 4. It can be observed that course 136 has the lowest percent of total defects for the steered portion of the 1270 *mm* radius courses and course 145 for the 635 *mm* radius courses. Relating the quality to the process parameters, it can be determined that low speed (20%), intermediate compaction (600 N), and a heater voltage of 170 V resulted in the best layup quality for the 1270 *mm* steered arcs. For the 635 *mm* courses, it is observed that a high-voltage

setting resulted in a better layup quality. Finally, comparing the quantity of defects between the courses steered at 1270 and 635 mm, it can be deduced that the number of defects increases with decreasing the steering radius.

4. Analysis of Defect Production

With a complete description of defect production across any given course in the experimental set, strong statistical links back to the processing parameters can be made. For each defect measurement at a given place on the course, a respective series of processing parameters at that point can be determined. Thus, it becomes possible to perform analysis on the influence of each processing parameter to overall defect production.

4.1. Feature Ranking

There is some debate in the AFP community as to the relative importance of each processing parameter in affecting the end quality of the layup. Answering this question is important for three reasons: (1) feature importance is an indication of underlying physics, (2) the relative importance of processing parameters can inform rule-of-thumb for manufacturing, and (3) eliminating trivial features is an important first step in building predictive models for defect production. For the data presented in this study, all processing parameters were analyzed using the RReliefF algorithm to determine the relative importance of each process parameter as input into the AFP system. The set of input features includes all parameters relevant to defect production on each steered course. Figure 22 shows all of the relevant features measured over the length of course 138 with the exception of pressure due to it being a constant.

4.1.1. RReliefF Algorithm

RReliefF [35] is an extension of the Relief Algorithm to continuous solution space ℓ with n-features. This family of algorithms provide a measurement of the variation in a response due to a specific feature. In general, RReliefF is attempting to determine for each feature the probability that an attribute A

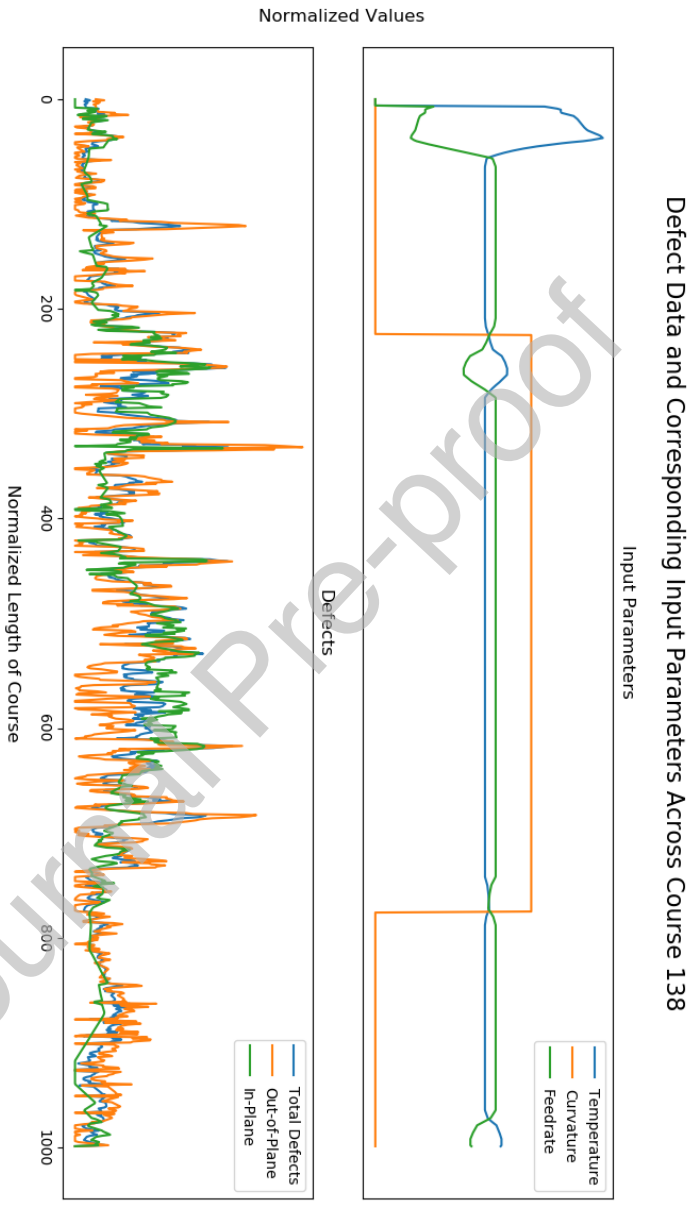

Figure 22: The Set of Input Features and Defects over the Length of Course 138 Excluding Pressure

Course	Out-of-plane (%)	In-plane (%)	Total (%)
130	6.450299682	7.512725898	13.96302558
131	3.693974769	12.67344951	16.36742428
132	5.950792835	10.79281393	16.74360677
133	5.258486948	6.133147523	11.39163447
134	4.993494061	11.1641179	16.15761196
135	5.189613028	10.1183946	15.30800763
136	5.365952658	4.593783067	9.959735725
137	10.10426455	8.577742049	18.6820066
138	7.449820927	10.23219371	17.68201463
139	9.855482566	14.33027596	24.18575852
140	10.3591335	12.34439332	22.70352681
141	10.56207866	11.28042102	21.84249968
142	8.716623498	18.73904474	27.45566824
143	10.41866851	9.731803273	20.15047179
144	12.18960178	16.38049785	28.57009963
145	8.740874378	7.274809729	16.01568411
146	8.202170736	9.490939012	17.69310975
147	12.94637567	20.8029705	33.82284229
149	10.2056666	12.55277019	22.75843678
150	10.55127462	13.02424192	23.57551654
151	12.67842508	11.56185289	24.24027796
152	10.35486105	8.111133449	18.4659945
153	13.47447483	7.601208133	21.07568296
154	14.7647512	11.78584303	26.55059423
155	8.850859631	10.21410145	19.06496108

Table 4: Areal percentage of defects for the steered portion of the courses

in a given instance is similar to A in a nearby instance. For a given set of

Parameter	Total Defects	Out-of-Plane	In-Plane
Pressure	$6.45 \cdot 10^{-4}$	$4.93 \cdot 10^{-4}$	$4.08 \cdot 10^{-4}$
Temperature	$4.88 \cdot 10^{-4}$	$2.61 \cdot 10^{-4}$	$4.73 \cdot 10^{-4}$
Curvature	$812 \cdot 10^{-2}$	$6.87 \cdot 10^{-2}$	$6.22 \cdot 10^{-2}$
Feedrate	$-8.11 \cdot 10^{-7}$	$-2.20 \cdot 10^{-5}$	$-2.73 \cdot 10^{-6}$

Table 5: RReliefF Quality Metric for Each Process Parameter and Defect Type

predictions τ, a weight $W[A]$ is assigned for every feature such that

$$W[A] = \sum_{I1,I2} similarity(\tau, I1, I2) \cdot similarity(A, I1, I2) \tag{4}$$

where $I1, I2 \in \ell$. This similarity function is best represented as a generalized difference between two points in the set. RReliefF and its variants provide a quality ranking of each feature in the set ranging from -1 to 1 [36] with -1 being the worst weighting and 1 being the best. RReliefF offers a number of unique advantages: namely that there is no independence requirement between features, the construction of the similarity function can be used to remove the need for normalization, and the algorithm itself is computationally inexpensive compared to other filter-based feature ranking methods. The RReliefF Algorithm is presented in the appendix.

The RReliefF algorithm is applied to our dataset with each parameter included as a feature in the analysis with each defect type measurement as the τ target. For our finalized set of process parameters, the RReliefF code generated a series of feature rankings indicating the significance of each input parameter [Table 5]. Figure 23 demonstrates a visualization of this.

4.2. Statistics

The development of the process parameter ranking from the RReliefF algorithm can be further validated through the examination of r and r^2 metrics

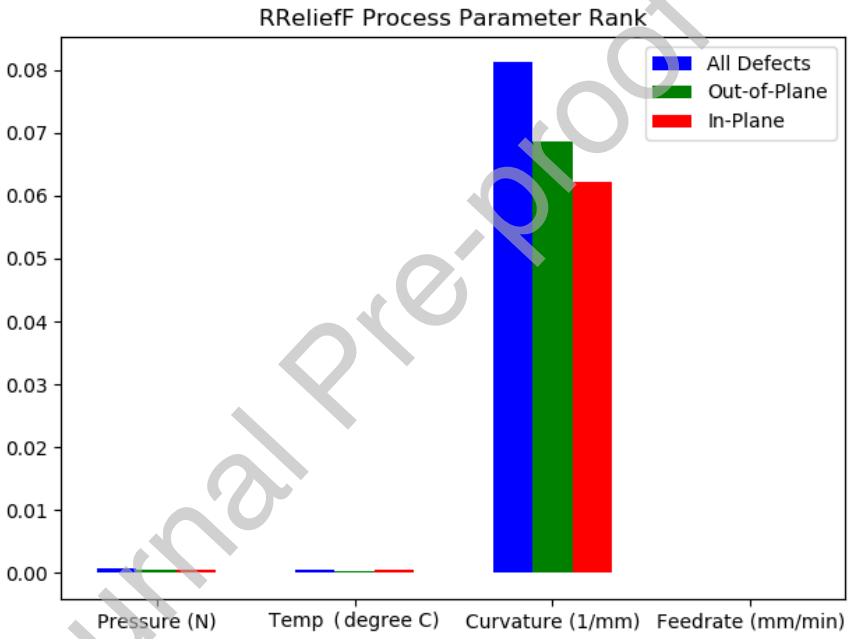

Figure 23: RReliefF Quality Feature Rankings for the Total Dataset

calculated across our dataset. Correlation coefficient is a metric by which the linear strength of a relationship between two sets of data can be measured. Where a correlation matrix is calculated, there is an implicit independence assumption between disparate sets of features, i.e. the interaction from additional features is not included in the calculation of the correlation coefficient between two features. The sign of the coefficient indicates the directionality of the relationship. A positive correlation coefficient indicates that an increase in one variable coincides with the increase in another variable. Negative or Anti-correlation indicates that an increase in one variable coincides with a decrease in another variable. The coefficient of determination, or r^2 is simply the square of the correlation coefficient and is a raw strength measurement without directionality. It can be clearly seen that the strongest correlations relate to curvature. While other parameters are weakly correlated with defect production, their influence is considerably less than the steering radius [Figure 24].

The high degree of influence derived from the curvature may obscure some trends. To address this, correlation and covariance measures are presented in for every curvature, effectively generating a subset of statistics removing the influence of curvature on defects, looking at each curvature as an independent dataset and deriving trends from the subset. The correlations from the 635mm radius courses can be seen in Figure 25. The correlation trends and RReliefF scores can be found in Section 8.

It can be seen in some instances that the correlation coefficients and RReliefF metrics appear to show two different trends in the data. Importantly, while the correlation coefficent measures the linear relationship between data, the RReliefF algorithm has no independence assumption, and can therefore account for interactions that would otherwise be unobserved. Just as importantly, while RReliefF can account for interactions that may exist between variables, it makes no statements on given trends between two variables like the correlation coefficient is capable of.

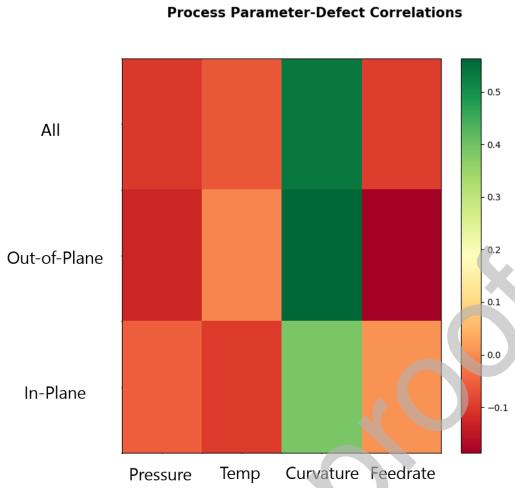

(a) Correlation Coefficient of Parameters and Defect Production

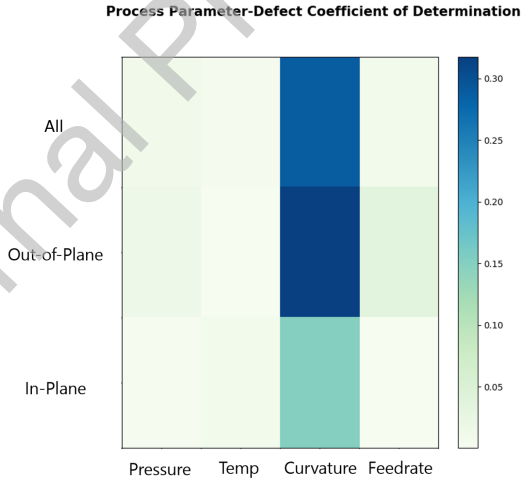

(b) r^2 Coefficient of Parameters and Defect Production

Figure 24: Correlation Statistics of Defect Production

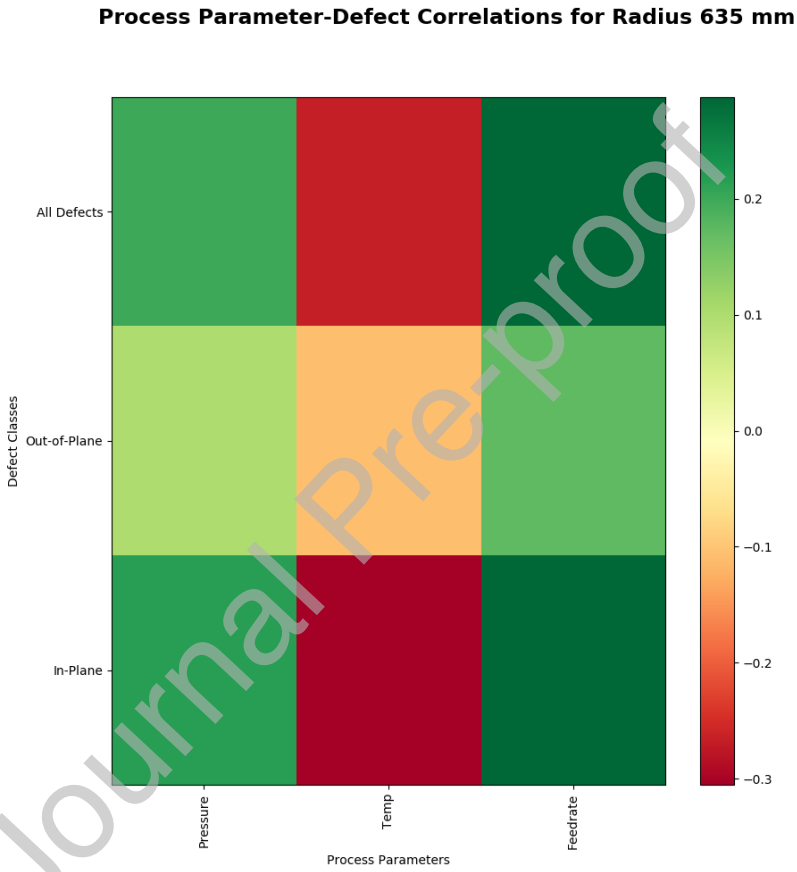

Figure 25: Removal of Curvature Influence by Examining Correlation Coefficient for the Aggregate Data of All 635 mm Courses

4.3. Notable Trends

It should also be noted that, while weakly correlated, the effects of speed on layup quality is not as simple of a linear relationship as an increase in speed increases defect production. While the correlation coefficient between speed and defect production remains strong across several curvatures, the modeling of variable interactions from RReliefF apply the lowest ranking to speed among almost all of the curvature types and the total dataset. The correlation measurement is at least an indication that the curvature considerations, a principle function of design, is a far greater influence than the layup speed itself. However, it should be noted that layup speed may be ultimately machine limited, indicating that trials on several different types of AFP machines may be required to definitively make a statement as to the true influence of speed on layup quality. In addition, the steering regimes explored in this study would be considered very high compared to both industry and previous experiments performed in the literature. For the initial experiments presented in this document that were performed at the McNair Center for Aerospace Innovation, it would seem to be indicated that speed effects could be compensated for by the increased application of temperature and pressure for high degrees of steering.

5. Conclusions

In this paper, the effect of the process parameters on the induced defects during steering of carbon fiber tows over a cylindrical surface using AFP were investigated. Three sets of nine steered paths at 1270, 635 and 318 mm are placed over a 1219 mm diameter cylindrical tool. It should be noted that these are very high rates of steering compared to the existing literature. The main process parameters investigated in this paper are the layup speed, temperature, and roller compaction. Each course was laid with a different set of the process parameters while monitoring the substrate temperature and the actual layup speed. Several steering induced defects appeared during the layup and are classified under two categories: large out-of-plane deformation (wrinkles, folds, and

sheared tows), and in-plane displacement (fiber waviness, tow bunching, and gaps). Images of the manufactured layups are acquired using profilometry scanning. These images were analyzed, and in-plane and out-of-plane defects were quantified for each course. Relationships between manufacturing and design parameters for each course were observed through the matching of parameter values at each point in the layup to defect production. RReiliefF feature ranking algorithms were used to determine the importance of each parameter, with curvature having a large effect on defect production. To remove the influence of course geometry from the analysis, a breakdown of each curvature type was also provided with correlation coefficients, covariances, and RReliefF metrics for each curvature. Key course geometry indicators including course center line were also reconstructed from minimal input from the reference design.

This study presents several notable observations. From the data acquisition section, it can be seen that compaction pressure has minimal influence on the nip point temperature. There is also a non-linear relationship between maximum nip-point temperature and the layup speed. From the analysis, it was determined that the single most important feature in the production of defects is the curvature of the course. However, it should be emphasized that the curvatures of steering involved in this study were high, implying that new relationships between curvature and defect could be observed at lower steering radii. In addition, it was observed that RReliefF rankings applied to both the entire dataset and by-curvature analysis applied low feature rankings to layup speed, indicating that higher speeds may potentially be overcome through the applications of higher temperature and pressure. Temperature is consistently negatively correlated with defect production, indicating that as temperature goes up, defect rates decrease.

If the importance of processing parameters were to be placed in order of importance from the observations of this study for the construction of composite parts with high rates of steering, the authors would list as follows:

- 1. Curvature

- 2. Temperature, Pressure
- 3. Feedrate

5.1. Future Work

Future work includes the identification of optimal processing windows using the data generated from these experiments as well as the application of this methodology to other material types including thermoplastics. It should be noted that for our analysis, an independence assumption was used between each input vector. It is a desire of the authors to expand the analysis to include the effects of defect production earlier in the course. In addition, there exists an opportunity to explore beyond constant curvature steered courses, with the analysis of defect production in variable curvature courses a logical next addition to this work. In the design of these variable curvature paths, an exploration of lower steering radii will be included.

6. Acknowledgment

All materials and access to the Lynx® AFP facility provided by the McNair Aerospace Center, University of South Carolina is gratefully acknowledged. The support and assistance of the McNair technical staff and undergraduate research students, particularly Andrew Anderson during operation of the AFP, and Matthew Godbold during the data processing is also greatly appreciated.

7. Data Availability

The raw/processed data required to reproduce these findings cannot be shared at this time as the data also forms part of an ongoing study.

References

[1] G. Rousseau, R. Wehbe, J. Halbritter, R. Harik, Automated Fiber Placement Path Planning: A state-of-the-art review, Computer-Aided Design

and Applications 16 (2) (2018) 172–203. doi:10.14733/cadaps.2019.172-203.

[2] A. W. Blom, P. B. Stickler, Z. Gürdal, Optimization of a composite cylinder under bending by tailoring stiffness properties in circumferential direction, Composites Part B: Engineering 41 (2) (2010) 157–165. doi:10.1016/j.compositesb.2009.10.004.
URL http://dx.doi.org/10.1016/j.compositesb.2009.10.004https://linkinghub.elsevier.com/retrieve/pii/S1359836809001887

[3] A. Khani, M. Abdalla, Z. Gürdal, Circumferential stiffness tailoring of general cross section cylinders for maximum buckling load with strength constraints, Composite Structures 94 (9) (2012) 2851–2860. doi:10.1016/j.compstruct.2012.04.018.
URL https://linkinghub.elsevier.com/retrieve/pii/S026382231200178X

[4] B. F. Tatting, Analysis and Design of Variable Stiffness Composite Cylinders, Ph.D. thesis, Virginia Polythecnic Institute and State University (1998).
URL https://theses.lib.vt.edu/theses/available/etd-10198-11378/unrestricted/Thesis.pdf

[5] M. Rouhi, H. Ghayoor, J. Fortin-Simpson, T. T. Zacchia, S. V. Hoa, M. Hojjati, Design, manufacturing, and testing of a variable stiffness composite cylinder, Composite Structures 184 (September 2017) (2018) 146–152. doi:10.1016/j.compstruct.2017.09.090.

[6] M. Sun, M. W. Hyer, Use of Material Tailoring to Improve Buckling Capacity of Elliptical Composite Cylinders, AIAA Journal 46 (3) (2008) 770–782. doi:10.2514/1.32495.
URL https://arc.aiaa.org/doi/10.2514/1.32495

[7] M. A. Albazzan, R. Harik, B. F. Tatting, Z. Gürdal, A. W. Blom-Schieber, M. Rassaian, S. P. Wanthal, Optimization of cylinders with holes under

bending using nonconventional laminates, in: AIAA/ASCE/AHS/ASC Structures, Structural Dynamics, and Materials Conference, 2018, no. 210049, American Institute of Aeronautics and Astronautics Inc, AIAA, 2018. doi:10.2514/6.2018-1377.

[8] M. Albazzan, B. Tatting, R. Harik, Z. Gürdal, A. Blom-Schieber, M. Rassaian, S. Wanthal, Design of Variable Stiffness Cylinder with Holes Under Bending for Maximum Buckling Load Using Lamination Parameters, SAMPE 2019 Conference & Exhibition, Charlotte, North Carolina, US, 20 – 23 May 2019 (2019) 1–18doi:10.33599/nasampe/s.19.1378.

[9] R. Harik, C. Saidy, S. J. Williams, Z. Gurdal, B. Grimsley, Automated fiber placement defect identity cards: Cause, anticipation, existence, significance, and progression, in: International SAMPE Technical Conference, Vol. 2018-May, Long Beach, California, 2018.

[10] R. Wehbe, B. Tatting, Z. Gürdal, R. Harik, Fiber Tow Deformations During Layup of Steered Paths Using Automated Fiber Placement Process, in: SAMPE 2019 - Charlotte, NC, SAMPE, 2019. doi:10.33599/nasampe/s.19.1591.
URL https://sampe.knack.com/technical-papers{#}home/technicalpaperdetails/5cb7823071efac0cb6e45a9e/

[11] R. Y. Wehbe, R. Harik, Z. Gurdal, In-plane tow deformations due to steering in automated fiber placement, in: AIAA Scitech 2019 Forum, American Institute of Aeronautics and Astronautics, Reston, Virginia, 2019. doi:10.2514/6.2019-1271.
URL https://arc.aiaa.org/doi/10.2514/6.2019-1271

[12] S. Rajan, M. A. Sutton, R. Wehbe, B. Tatting, Z. Gürdal, A. Kidane, R. Harik, Experimental investigation of prepreg slit tape wrinkling during automated fiber placement process using StereoDIC, Composites Part B: Engineering 160 (December 2018) (2019) 546–557. doi:10.1016/j.compositesb.2018.12.017.

URL https://doi.org/10.1016/j.compositesb.2018.12.017https://linkinghub.elsevier.com/retrieve/pii/S1359836818323461

[13] R. Wehbe, B. Tatting, S. Rajan, R. Harik, M. Sutton, Z. Gürdal, Geometrical modeling of tow wrinkles in automated fiber placement, Composite Structures 246 (2020) 112394. doi:10.1016/j.compstruct.2020.112394.
URL https://linkinghub.elsevier.com/retrieve/pii/S0263822320302324

[14] N. Bakhshi, M. Hojjati, An experimental and simulative study on the defects appeared during tow steering in automated fiber placement, Composites Part A: Applied Science and Manufacturing 113 (2018) 122–131. doi:10.1016/j.compositesa.2018.07.031.
URL https://linkinghub.elsevier.com/retrieve/pii/S1359835X1830280X

[15] R. Smith, Z. Qureshi, R. Scaife, H. El-Dessouky, Limitations of processing carbon fibre reinforced plastic/polymer material using automated fibre placement technology, Journal of Reinforced Plastics and Composites 35 (21) (2016) 1527–1542. doi:10.1177/0731684416659544.
URL http://journals.sagepub.com/doi/10.1177/0731684416659544

[16] C. Zhao, J. Xiao, W. Huang, X. Huang, S. Gu, Layup quality evaluation of fiber trajectory based on prepreg tow deformability for automated fiber placement, Journal of Reinforced Plastics and Composites 35 (21) (2016) 1576–1585. doi:10.1177/0731684416659933.
URL http://journals.sagepub.com/doi/10.1177/0731684416659933

[17] G. Clancy, D. Peeters, V. Oliveri, D. Jones, R. M. O'Higgins, P. M. Weaver, A study of the influence of processing parameters on steering of carbon Fibre/PEEK tapes using laser-assisted tape placement, Composites Part B: Engineering 163 (October 2018) (2019) 243–251. doi:10.1016/j.compositesb.2018.11.033.
URL https://doi.org/10.1016/j.compositesb.2018.11.033

[18] A. B. Radwan, Experimental Analysis of the Automated Fiber Placement Manufacturing Parameters for High and Low Tack Prepreg Material, Master thesis, University of South Carolina (2019).
URL https://scholarcommons.sc.edu/cgi/viewcontent.cgi?article=6431{&}context=etd

[19] S. G. Pickering, K. Chatterjee, D. P. Almond, S. Tuli, LED optical excitation for the long pulse and lock-in thermographic techniques, NDT and E International 58 (2013) 72–77. doi:10.1016/j.ndteint.2013.04.009.
URL http://dx.doi.org/10.1016/j.ndteint.2013.04.009

[20] I. Jorge Aldave, P. Venegas Bosom, L. Vega González, I. López De Santiago, B. Vollheim, L. Krausz, M. Georges, Review of thermal imaging systems in composite defect detection, Infrared Physics and Technology 61 (2013) 167–175. doi:10.1016/j.infrared.2013.07.009.
URL http://dx.doi.org/10.1016/j.infrared.2013.07.009

[21] V. Kalyanavalli, T. K. Ramadhas, D. Sastikumar, Long pulse thermography investigations of basalt fiber reinforced composite, NDT and E International 100 (December 2017) (2018) 84–91. doi:10.1016/j.ndteint.2018.08.007.
URL https://doi.org/10.1016/j.ndteint.2018.08.007

[22] E. Hu, F. Haifeng, Surface profile inspection of a moving object by using dual-frequency Fourier transform profilometry, Optik 122 (14) (2011) 1245–1248. doi:10.1016/j.ijleo.2010.08.007.
URL http://dx.doi.org/10.1016/j.ijleo.2010.08.007

[23] C. Sacco, A. B. Radwan, R. Harik, M. Van Tooren, Automated fiber placement defects: Automated inspection and characterization, in: International SAMPE Technical Conference, Vol. 2018-May, 2018.

[24] C. Sacco, A. B. Radwan, T. Beatty, R. Harik, Machine Learning Based AFP Inspection : A Tool for Characterization and Integration, SAMPE Conference Proceedings.

[25] C. Sacco, Machine Learning Methods for Rapid Inspection of Automated Fiber Placement Manufactured Composite Structures, Master thesis, University of South Carolina (2019).

[26] E. D. Gregory, P. D. Juarez, In-situ thermography of automated fiber placement parts, in: AIP Conference Proceedings, 2018. doi:10.1063/1.5031551.

[27] P. D. Juarez, E. D. Gregory, In situ thermal inspection of automated fiber placement manufacturing, in: AIP Conference Proceedings, 2019. doi:10.1063/1.5099847.

[28] J. Cemenska, T. Rudberg, M. Henscheid, Automated In-Process Inspection System for AFP Machines, SAE International Journal of Aerospacedoi:10.4271/2015-01-2608.

[29] D. Maass, Progress in automated ply inspection of AFP layups, Reinforced Plastics 59 (5) (2015) 242–245. doi:10.1016/j.repl.2015.05.002.
URL http://dx.doi.org/10.1016/j.repl.2015.05.002

[30] T. Rudberg, J. Nielson, M. Henscheid, J. Cemenska, Improving AFP Cell Performance, SAE International Journal of Aerospacedoi:10.4271/2014-01-2272.

[31] R. Wehbe, Modeling of Tow Wrinkling in Automated Fiber Placement based on Geometrical Considerations, Master thesis, University of South Carolina (2017).

[32] C. Maple, Geometric design and space planning using the marching squares and marching cube algorithms, in: Proceedings - 2003 International Conference on Geometric Modeling and Graphics, GMAG 2003, 2003. doi:10.1109/GMAG.2003.1219671.

[33] M. Erwig, The graph Voronoi diagram with applications, Networksdoi:10.1002/1097-0037(200010)36:3<156::AID-NET2>3.0.CO;2-L.

[34] K. Rohila, P. Gouthami, P. M, Dijkstra ' s Shortest Path Algorithm, International Journal of Innovative Research in Computer and Communication Engineering.

[35] M. Robnik-Sikonja, I. Kononenko, Theoretical and Empirical Analysis of ReliefF and RReliefF, Machine Language 53 (2003) 23–69. doi:10.1023/A:1025667309714.

[36] R. J. Urbanowicz, M. Meeker, W. La Cava, R. S. Olson, J. H. Moore, Relief-based feature selection: Introduction and review, Journal of Biomedical Informatics 85 (January) (2018) 189–203. arXiv:1711.08421, doi:10.1016/j.jbi.2018.07.014.
URL https://doi.org/10.1016/j.jbi.2018.07.014

8. Appendix

8.1. RReliefF Algorithm

The RReliefF algorithm and some notes on the implementation in this study is presented bellow.

Data: A vector of features R and response values $\tau(x)$

Result: Vector W of estimations of the qualities of each feature A

$N_{dC}, N_{dA}[A], N_{dC\&dA}[A], W[A] \rightarrow 0$;

for $i = 1$ *to* m **do**

  get random instance R_i;

  select k instances I_j nearest to R_i;

  for $j = 1$ *to* k **do**

    $N_{dC} \rightarrow N_{dC} + diff(\tau, R_i, I_j) \cdot d(i, j)$;

    for $A = 1$ *to* a **do**

      $N_{dA}[A] \rightarrow N_{dA}[A] + diff(A, R_i, I_j) \cdot d(i, j)$;

      $N_{dC\&dA}[A] \rightarrow$

      $N_{dC\&dA}[A] + diff(\tau, R_i, I_j) \cdot diff(A, R_i, I_j) \cdot d(i, j)$;

    end

  end

end

for $A = 1$ *to* a **do**

  $W[A] = \frac{N_{dC\&dA}[A]}{N_{dC}} - \frac{N_{dA}[A] - N_{dC\&dA}[A]}{m - N_{dC}}$

end

Algorithm 1: RReliefF Pseudocode

$diff$ is a generalized distance function. In the case of this study, it is set to

$$diff(F, R, I) = \begin{cases} 0 & |F[R] - F[I]| = 0 \\ 1 & |F[R] - F[I]| \geq max(F) - min(F) \\ \frac{|F[R] - F[I]|}{max(F) - min(F)} & otherwise \end{cases} \tag{5}$$

8.2. RReliefF Scores by Radius

A series of tables showing correlations, covariances, and RReliefF rankings for individual curvature sets is displayed bellow.

Parameter	Total Defects	Out-of-Plane	In-Plane
Pressure	0	0	0
Temperature	$1.33 \cdot 10^{-3}$	$4.28 \cdot 10^{-4}$	$4.00 \cdot 10^{-4}$
Feedrate	$-9.15 \cdot 10^{-5}$	$-3.75 \cdot 10^{-7}$	$-9.12 \cdot 10^{-5}$

Table 6: RReliefF Quality Metrics for Radius 318mm

Parameter	Total Defects	Out-of-Plane	In-Plane
Pressure	$-2.48 \cdot 10^{-5}$	$-5.49 \cdot 10^{-5}$	$1.24528 \cdot 10^{-4}$
Temperature	$1.91 \cdot 10^{-4}$	$1.14 \cdot 10^{-4}$	$3.50 \cdot 10^{-4}$
Feedrate	$-1.7124 \cdot 10^{-4}$	$-9.67 \cdot 10^{-5}$	$-4.73 \cdot 10^{-5}$

Table 7: RReliefF Quality Metrics for Radius 635mm

Parameter	Total Defects	Out-of-Plane	In-Plane
Pressure	$5.57 \cdot 10^{-3}$	$4.99 \cdot 10^{-3}$	$3.84 \cdot 10^{-3}$
Temperature	$1.48 \cdot 10^{-2}$	$6.38 \cdot 10^{-3}$	$2.25 \cdot 10^{-2}$
Feedrate	$1.84 \cdot 10^{-4}$	$1.36 \cdot 10^{-4}$	$1.76 \cdot 10^{-4}$

Table 8: RReliefF Quality Metrics for Radius 1270mm

Parameter	Total Defects	Out-of-Plane	In-Plane
Pressure	$3.06 \cdot 10^{-4}$	$5.20 \cdot 10^{-4}$	$7.44 \cdot 10^{-4}$
Temperature	$1.26 \cdot 10^{-3}$	$9.99 \cdot 10^{-4}$	$1.21 \cdot 10^{-3}$
Feedrate	$-9.89 \cdot 10^{-5}$	$-6.24 \cdot 10^{-5}$	$1.19 \cdot 10^{-4}$

Table 9: RReliefF Quality Metrics for Radius ∞

8.3. Correlation Coefficient by Radius

Parameter	Total Defects	Out-of-Plane	In-Plane
Pressure	−0.09	−0.03	−0.12
Temperature	−0.09	−0.10	−0.05
Feedrate	0.22	0.24	0.12

Table 10: Correlation Coefficient for Radius 318mm

Parameter	Total Defects	Out-of-Plane	In-Plane
Pressure	0.20	0.10	0.22
Temperature	−0.27	−0.11	−0.31
Feedrate	0.29	0.17	0.29

Table 11: Correlation Coefficient for Radius 635mm

Parameter	Total Defects	Out-of-Plane	In-Plane
Pressure	0.00	0.20	−0.15
Temperature	−0.21	0.06	−0.34
Feedrate	0.21	−0.04	0.32

Table 12: Correlation Coefficient for Radius 1270mm

Parameter	Total Defects	Out-of-Plane	In-Plane
Pressure	0.04	0.04	0.02
Temperature	−0.05	−0.02	−0.06
Feedrate	0.01	0.02	−0.01

Table 13: Correlation Coefficient for Radius ∞

8.4. Covariance by Radius

Parameter	Total Defects	Out-of-Plane	In-Plane
Pressure	−1.035711358	−0.221178151	−0.814533208
Temperature	−0.144768168	−0.099472606	−0.045295562
Feedrate	26.2509451	17.28597275	8.964972352

Table 14: Covariances for Radius 318mm

Parameter	Total Defects	Out-of-Plane	In-Plane
Pressure	4.240226098	1.040248786	3.190039974
Temperature	−4.163518118	−0.836853368	−3.324661091
Feedrate	64.55381875	19.39760121	45.18225232

Table 15: Covariances for Radius 635mm

Parameter	Total Defects	Out-of-Plane	In-Plane
Pressure	−0.027053034	1.344218001	−1.371271035
Temperature	−0.198797549	0.02792865	−0.226726199
Feedrate	77.38995847	−6.661258504	84.05121698

Table 16: Covariances for Radius 1270mm

Parameter	Total Defects	Out-of-Plane	In-Plane
Pressure	0.340866239	0.20771199	0.133154248
Temperature	−0.284711434	−0.063456966	−0.221254468
Feedrate	1.117169393	1.619964363	−0.50279497

Table 17: Covariances for Radius ∞

Declaration of interests

☒ The authors declare that they have no known competing financial interests or personal relationships that could have appeared to influence the work reported in this paper.

☐The authors declare the following financial interests/personal relationships which may be considered as potential competing interests: